Imaging of Cochlear Tissue With a Grating Interferometer and Hard X-Rays

CLAUS-PETER RICHTER,[1,2,3]* STEPHANIE SHINTANI-SMITH,[1] ANDREW FISHMAN,[1] CHRISTIAN DAVID,[4] IAN ROBINSON,[5,6] AND CHRISTOPH RAU[1,6]

[1]*Department of Otolaryngology, Northwestern University Feinberg School of Medicine, Chicago, Illinois 60611*
[2]*Department of Biomedical Engineering, Northwestern University, Evanston, Illinois 60208*
[3]*Department of Communication Sciences and Disorders, Northwestern University, The Hugh Knowles Center, Evanston, Illinois 60208*
[4]*Laboratory for Micro- and Nanotechnology, Paul Scherrer Institut, 5232 Villigen PSI, Switzerland*
[5]*Department of Physics and Astronomy, University College, London WC1E 6BT, United Kingdom*
[6]*Diamond Light Source Ltd., Diamond House, Harwell Science and Innovation Campus, Didcot, Oxfordshire, OX11 0DE, United Kingdom*

KEY WORDS inline phase contrast; grating interferometer; soft tissue; cochlea; coherent

ABSTRACT This article addresses an important current development in medical and biological imaging: the possibility of imaging soft tissue at resolutions in the micron range using hard X-rays. Challenging environments, including the cochlea, require the imaging of soft tissue structure surrounded by bone. We demonstrate that cochlear soft tissue structures can be imaged with hard X-ray phase contrast. Furthermore, we show that only a thin slice of the tissue is required to introduce a large phase shift. It is likely that the phase contrast image of the soft tissue structures is sufficient to image the structures even if surrounded by bone. For the present set of experiments, structures with low-absorption contrast have been visualized using in-line phase contrast imaging and a grating interferometer. The experiments have been performed at the Advanced Photon Source at Argonne National Laboratories, a third generation source of synchrotron radiation. The source provides highly coherent X-ray radiation with high-photon flux ($>10^{12}$ photons/s) at high-photon energies (5–70 keV). Radiographic and light microscopy images of the gerbil cochlear slice samples were compared. It has been determined that a 20-μm thick tissue slice induces a phase shift between $1/3\pi$ and $2/3\pi$. *Microsc. Res. Tech. 72:902–907, 2009.*

INTRODUCTION

In clinical settings, hard X-rays have been used to image radiopaque materials such as bone. However, conventional radiography is drastically limited where the structures under investigation are weakly absorbing objects, including soft tissue. Radiological diagnostics could be improved if both, radiolucent and radiopaque tissue structures could be visualized simultaneously. Recently, new techniques have been introduced that can be used to image weakly absorbing soft tissue structures with hard X-rays. The novel techniques rely on contrast generated by the phase shift induced on the X-ray wavefront by the object (Momose et al., 1998; Rau et al., 2006; Snigirev et al., 1995; Spanne et al., 1999; Takeda et al., 1995, 2002a). Conventional techniques, on the other hand, rely on contrast generated by the absorption of the X-rays by the object.

The phase information of an object becomes apparent under coherent illumination. Examples of coherent radiation sources are synchrotrons, including the Advanced Photon Source (APS) at Argonne National Laboratory.

Recently, two and three-dimensional reconstructions of weakly absorbing materials have been produced using grating interferometers (Bunk et al., 2005; Guigay et al., 2004; Kottler et al., 2007; Pfeiffer et al., 2005, 2006a,b; Takeda et al., 2000, 2002b; Weitkamp et al., 2005; Yashiro et al., 2008). Similar to Pfeiffer and coworkers, we demonstrate with the present experiments that imaging of soft tissue with hard X-rays and a grating interferometer is possible (Pfeiffer et al., 2006a,b). This is an important step toward imaging soft cochlear tissues surrounded by bone. The radiation energy must be selected that the absorption from the bone is negligible but the phase shift of the tissue is large. We have determined that photon energies above 11 keV are little absorbed by the bone. However, it is unclear whether the phase shift of a thin layer forms an image with sufficient contrast. With the grating interferometer, we have been able to determine that thin layers of soft tissue structures can be imaged. We also could determine the phase shift induced by a thin cochlear tissue slice. With this novel method, we are able to examine cochlear micromechanics and it will be possible to quickly determine gross morphological changes present in mice with genetically induced hearing loss.

*Correspondence to: Claus-Peter Richter, Department of Otolaryngology, Northwestern University Feinberg School of Medicine, Searle Building 12-470, 303 E. Chicago Avenue, Chicago, IL 60611-3008, USA.
E-mail: cri529@northwestern.edu

Received 15 December 2008; accepted in revised form 26 March 2009

Contract grant sponsor: Frederick Seitz Materials Research Laboratory, University of Illinois at Urbana-Champaign; Contract grant number: DEFG02-91ER45439; Contract grant sponsor: ORNL; Contract grant number: DE-AC05-00OR22725; Contract grant sponsor: US DOE, Basic Energy Sciences, Office of Science; Contract grant number: W-31-109-ENG-38; Contract grant sponsor: NSF; Contract grant number: IBN-0415901; Contract grant sponsors: NIST (U.S. Department of Commerce), UOP LLC.

DOI 10.1002/jemt.20728

Published online 19 May 2009 in Wiley InterScience (www.interscience.wiley.com).

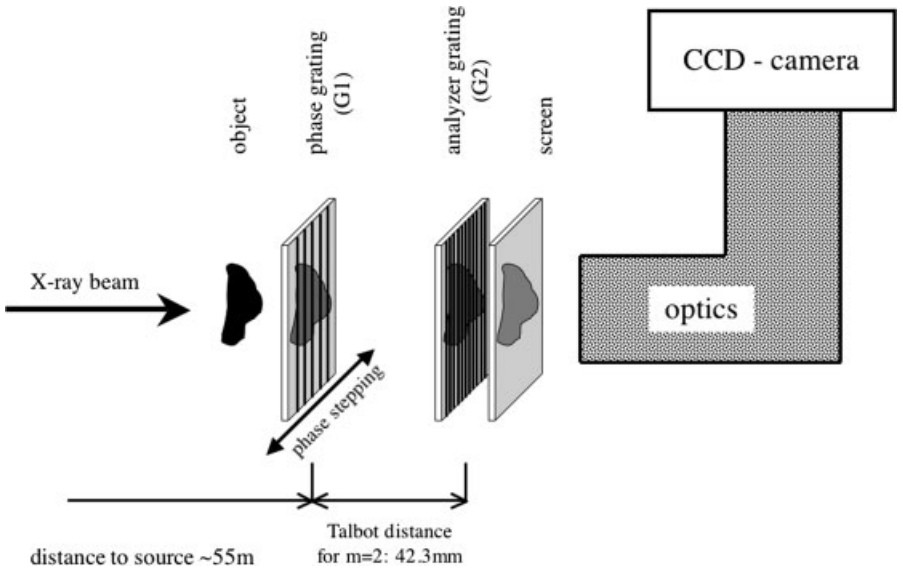

Fig. 1. The gratings and the probe were installed on a vibration-isolated table as indicated in the figure. After aligning the gratings and mounting the probe, the analyzer grating was stepped perpendicular to the axis of the X-ray beam as shown by the arrow and an image was captured for each step. The sample was mounted directly in front of the phase grating (G1) on a sample stage, which consisted of several high-quality stages for tilts, translations, and rotations. The phase grating (G1) was mounted on a stage that consisted of several high-quality stages for tilts and translations and the analyzer grating (G2) was placed directly in front of the scintillation screen. The scintillation screen transforms the X-rays into visible light, which is then projected via a microscope lens onto the chip of a CCD camera.

METHODS

Experimental Setup

The experiments were conducted at Argonne National Laboratory in the "C" hutch of 34ID at a distance of 55 m from the X-ray source. For the imaging, the gratings and the probe were installed on a vibration-isolated table (Fig. 1). The phase grating (G1) was mounted on a stage that consisted of several high-quality stages for tilts and translations. The analyzer grating (G2) was placed directly in front of the scintillation screen. The sample was mounted on a sample stage directly in front of the phase grating (G1). The sample stage consisted of several high-quality stages for tilts, translations, and rotations. The radiation intensity transmitted through the sample and the gratings was recorded with a CCD-based detector. The scintillation screen of the detector transforms the X-rays into visible light, which is then projected via a microscope lens onto the chip of a CCD camera. After aligning the gratings and mounting the probe, the phase grating was stepped perpendicular to the axis of the X-ray beam and an image was captured for each position of the grating.

The Radiation Source

The experiments were conducted at the APS at Argonne National Laboratory at 34ID-C. The APS is a synchrotron radiation source of the third generation, for which the particular characteristic is highly coherent X-ray radiation. X-rays are generated with an undulator, inserted in a straight section of the storage ring. The full width half maximum source size is 600 μm by 40 μm (horizontal × vertical) and the beam divergence is 40 μrad by 12 μrad (horizontal × vertical). At 34ID, the beam is shared between two different hutches. The beam splitting is achieved by inserting a platinum-coated silicon single-crystal mirror into the beam, deflecting most of the central cone of the X-ray beam to the C hutch. The liquid nitrogen-cooled mirror rejects undulator harmonics above 15 keV at an incidence angle of 5 mrad. The fixed-exit, double-crystal monochromator is water-cooled and yields an energy bandwidth of $\Delta E/E = 10^{-4}$ using Si (111) crystals over an energy range of 6–30 keV. The beam size is $\sim$1 mm^2 at a distance of 55 m from the source and the monochromatic flux is about 10^{12} photons/s.

The Grating Interferometer

Imaging of low-absorbing materials with hard X-rays and a grating interferometer constitute a new approach for phase contrast imaging (David et al., 2002; Pfeiffer et al., 2005; Takeda et al., 2000; Weitkamp et al., 2005; Yashiro et al., 2008). The interferometer consists of two linear grids or gratings, a phase grating (G1) and an analyzer grating (G2). The phase grating (G1) has lines with negligible absorption and introduces a significant phase shift to the wavefront. At certain distances, the so-called Talbot distances, the propagating wave field forms periodic fringes with maximum contrast. This self-image of the grating has doubled pitch frequency. An object in the beam, positioned just in front of the phase grating, causes perturbations of the incident wavefront and results in local displacement of the fringes. By detecting the position of the fringes, it is possible to reconstruct the object. Because the pitch of the fringe spacing is generally smaller than the size of a detector pixel, a scintillation screen placed in the detection plane will generally not have sufficient resolution to resolve the fringes and form an image. Therefore, a grating (G2) with absorb-

ing lines with the same periodicity and orientation as the fringes are placed in the detection plane directly in front of the detector. Grating (G2) serves as a transmission mask for the detector and transforms local fringe positions into signal intensity variations. In other words, the detected signal profile contains quantitative information about the phase gradient of the object.

For the experiments, the silicon phase grating (G1) was 11-μm thick. The phase shift of the grating is π for 8.75 keV photon energy (λ = 1.417 Å). The grating's pitch p was 4 μm and the distance for the maxima was calculated as follows:

$$d_m = (m - \frac{1}{2})\frac{p^2}{4\lambda}, \quad (1)$$

where d denotes the Talbot distance, m the integer number of the maximum, p the pitch of the grating, and λ the wavelength of the radiation. The Talbot distance for the second maximum was experimentally determined. It was 42.3 mm, which corresponds with the calculated value.

The gold analyzer grating (G2) had a pitch of 2 μm and was 10-μm thick.

Phase Stepping

To separate the phase information from other contributions to the signal, the phase grating was scanned along the transverse direction (Pfeiffer et al., 2005, 2006b; Weitkamp et al., 2005). The scanning distance was 4 μm, which corresponds two periods of the grating. After each step (42 steps per scan, at step width of 100 nm) an image was captured. The intensity of the signal $I(x, y)$ in each pixel (x, y) oscillates as a function of the position of the analyzer grating. The intensity changes of the pixels in one image line are plotted in an oscillation map. In the oscillation maps, the x-axes denote the number of the pixel along the x-axis of the image and the y-axis denotes the number of steps in the scan. The phase $\varphi(x, y)$ of the intensity oscillations in each pixel is related to the wavefront phase profile $\Phi(x, y)$, the X-ray wavelength λ, the distance d between the two gratings, and the period g_2 of the absorption grating by

$$\varphi = \frac{\lambda d}{g_2}\frac{\partial \Phi}{\partial x}. \quad (2)$$

The phase $\varphi(x, y)$ thus contains only the objects phase information, particularly excluding the absorption contrast. The phase profile of the object can thus be retrieved from $\varphi(x, y)$ by a simple one-dimensional integration along the x-axis of the phase image.

Radiation Dose

When hard X-rays are used, it is important to ensure that the tissue is not damaged by the radiation dosage applied. When determining the radiation dose, several factors have to be considered: the photon energy spectrum and the properties of the absorbing medium. The theoretical description is generally complex for photons because the dose is delivered by recoiling charged particles in the medium, which have a spread of energies and directions. The dose can be calculated using the electron-mass-absorption coefficient and the following equation:

$$D = \Phi E \frac{\mu}{\rho}, \quad (3)$$

where D denotes the absorbed energy per mass, Φ the photon flux, E the photon energy, and μ/ρ the mass-energy-absorption coefficient. According to the results from XMuDat (http://www-nds.iaea.org/reports/nds-195.htm) the electron-mass-absorption coefficient for muscle tissue is 6.8 cm^2/g. The dose calculates to 3.8 mGy per image. Note, the average radiation dose from an abdominal X-ray is 1.4 mGy.

Dissection of the Tissues

Cochlear slices were made as follows. After an intraperitoneal injection of a lethal dose of sodium pentobarbital (180 mg/kg body weight), gerbils were sacrificed. Following decapitation, the head was divided in the medial plane and the bullae were removed. Next, one of the bullae was opened and the cochlea was exposed and placed in 4% paraformaldehyde in 0.1 M phosphate-buffered saline (PBS), pH 7.4. After 2 h, the cochleae were rinsed in PBS and placed for 2 weeks in PBS containing 10% ethylenediamine tetraacedic acid, pH 7.4, at 4°C to decalcify. PBS was made from solutions of 0.2 M NaH_2PO_4 and 0.2 M Na_2HPO_4, to which 0.9% NaCl was added.

The cochleae were then prepared for sectioning on a cryostat by sucrose-embedding the tissue. The tissue was incubated in increasing concentrations of sucrose solution for 30 min at each step, while on a tissue rotator at room temperature (10% sucrose; 2:1 solution of 10:30% sucrose; 1:1 solution of 10:30% sucrose; 1:2 solution of 10:30% sucrose; 30% sucrose). Finally, specimens were stored overnight in 30% sucrose solution at 4°C. The next day, the cochleae were placed in degassed optimal temperature cutting compound (OCT, Tissue-Tek) and stored in OCT overnight at 4°C. The cochleae were frozen in OCT, using an ethanol and dry ice bath. Samples were stored at a temperature of −80°C until ready for sectioning.

For sectioning, the specimens were placed in the cryostat and allowed to equilibrate to the temperature of the cryostat (−20°C). The cochleae were oriented for sectioning parallel to the modiolus. The tissue specimens were cut at 20 μm and were mounted on biobond-coated superfrost microscope slides. After sectioning, the slides were allowed to air dry for 2 h.

For light microscopy, the slices were stained with a Toluidine blue/Tetraborate mixture (1:20); 1% Tetraborate in distilled water and 1% Toluidine in distilled water. After the staining, the specimen was covered with Paramount and 100 μm glass cover-slides.

Image Acquisition and Image Processing

The camera system consisted of a scintillation screen coupled via an optical microscope to a CCD detector. The scintillation screen transformed the X-rays into visible light, which was projected with an optical microscope onto the chip of a CCD camera (Kodak KX2e). The camera had 14-bit resolution with a 1560 × 1024 pixel array and 9 × 9 μm^2 size of each pixel. Using

a 20× objective lens (Mitutoyo) the effective pixel size on the screen was 0.45 μm. The scintillation screen was an Yttrium Aluminum Garnet single crystal with a 6-μm thick europium-doped active layer. With the earlier-mentioned elements, the camera system provided a spatial resolution of 2.4 μm (20× lens).

For all projections, additional images were taken: the "flat field" beam profile (without the sample) and a dark count image of the CCD without X-rays on the detector system (dark field). Heterogeneities of the beam profile were corrected using these additional images.

The image data were collected in HDF format, and converted to TIF format using an application custom written for IDL-6. Using the application ImageJ, a z-projection was created to summate individual phase interferometer images. Following X-ray imaging, the specimens were stained with toluidine blue, as described earlier, and photographed under the microscope.

RESULTS

It was possible to image 20-μm thick soft tissue slices using hard X-rays and a grating interferometer. In total 10 slices from three animals were used for imaging. Although little absorption of the radiation occurred, the phase shift induced by the soft tissue was large enough to visualize the structures of interest. Figure 2 shows a sample that has been imaged with X-rays and with light microscopy for comparison. Similar cochlear structures can be identified with both methods. The basilar membrane, the organ of Corti and Rosenthal's canal with spiral ganglion cells can be identified.

Oscillation Maps

Phase information was separated from other contributions to the signal, by scanning the phase grating along the transverse direction (see also Methods section). After each step (42 steps per scan) an image was captured. The 42 images captured during one scan were used to construct a novel image, the oscillation map. The construction of the oscillation map was started by selecting one image line in image 1 of the 42 images of the scan. This line was plotted as the first line of the new image. Subsequent images of the scan were then used. The corresponding image lines were selected and were plotted as subsequent lines of the new image, the oscillation map. Phase information can be directly obtained from the oscillation maps by identifying discontinuities. The intensity function is plotted for a selected image line (Fig. 3). As shown in Figure 4, a shift of the profile in the oscillation map occurs at places that show a soft tissue structure in the image. For example, the image edge at $(x, y) = (70, 41)$ in Figure 4A can be clearly identified in its corresponding oscillation map in Figure 4B. The shifted distance is proportional to the phase shift. To determine the local phase variation, the intensity modulation for two selected pixels $(x, y) = (60, 61)$ and $(x, y) = (130, 61)$ were plotted for the 42 step of a phase scan (Fig. 5). The intensity data obtained from the pixels data were fitted to a sinusoidal function. The phase was one of the fitting parameters and was used to calculate the phase difference between the two selected locations. In Figure 5, we can detect a displacement of the intensity curves in the x-direction, which corresponds to an π approximated 120° ($2/3\pi$) phase shift.

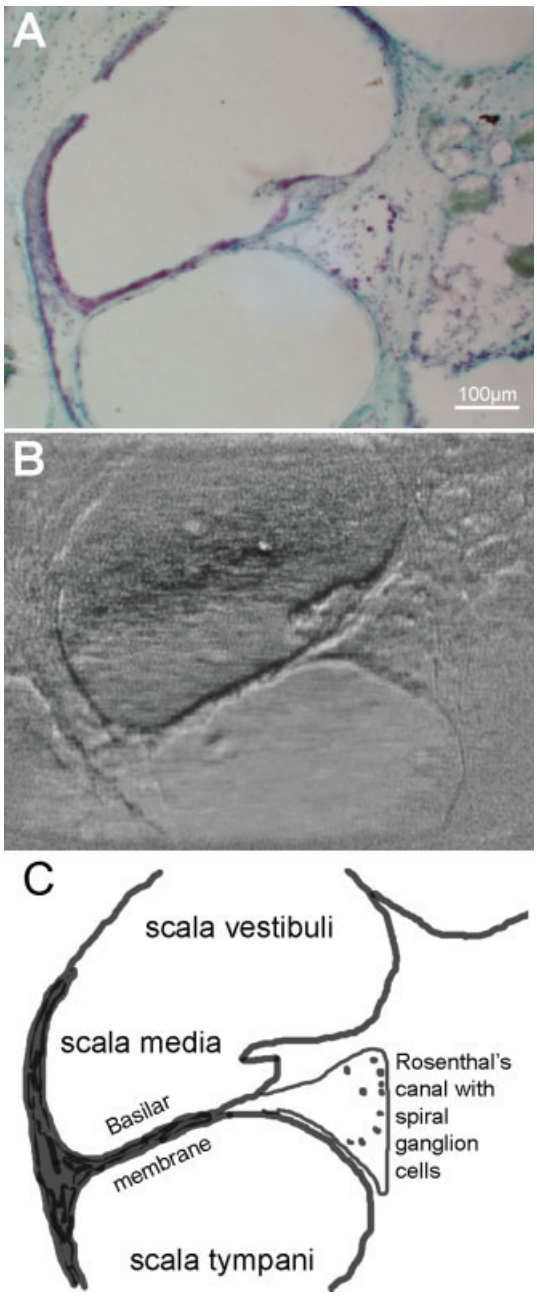

Fig. 2. Light microscopy (**A**) and X-ray montage (**B**) of a damaged cochlea with low number of spiral ganglion cells. (**C**) A sketch of the above images. Structures are labeled, including the basilar membrane and Rosenthal's canal, which holds the auditory nerve cells, the spiral ganglion cells. The cochlea has been treated with neomycin, an ototoxic drug. Therefore, only few spiral ganglion cells can be seen.

Phase information has also been retrieved more systematically for each neighboring pixel as described in Methods section. Local phase differences were calculated for neighboring pixels along the x-axis. The total phase change was calculated by integrating along the x-direction. For the example in Figure 6, the phase shift introduced by the 20-μm thick tissue slice was ~60°.

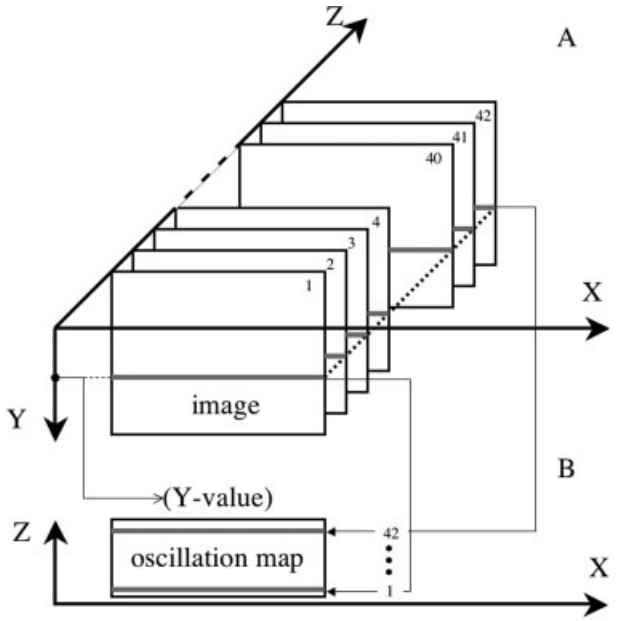

Fig. 3. Schematic construction of oscillation maps. To retrieve the phase information of the object, the phase grating is stepped along a horizontal axis perpendicular to the grids of the grating. At each of the 42 steps, an image is taken. The *x*- and *y*-axis are the axes of each of the images. The resulting images for the scan are stacked along the *z*-axis (**A**). The construction of the oscillation map is shown in (**B**): A line for one *y*-axis value is selected. Next, for each *x*-value, the corresponding 42 *z*-values are plotted.

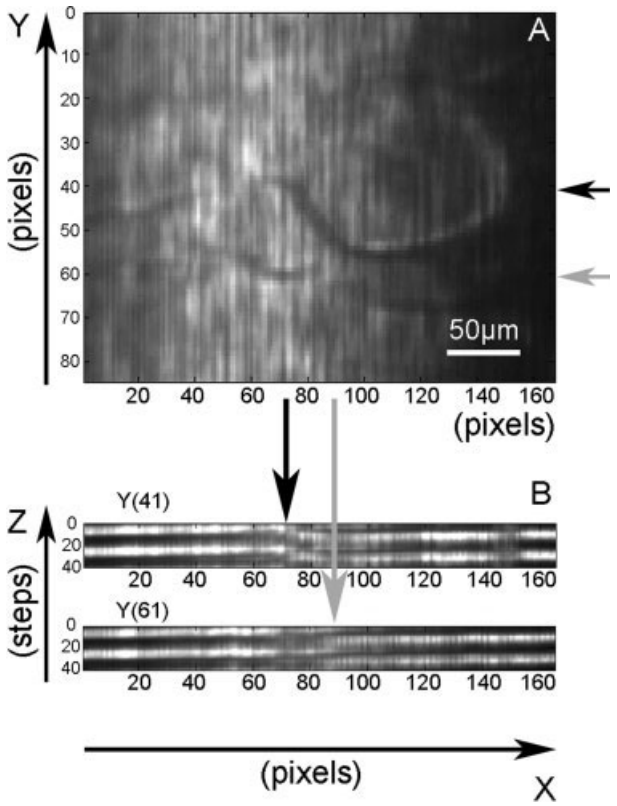

Fig. 4. (**A**) The image shows a cochlear cross section for an arbitrary constellation of the phase grating and the analyzer grating. Note that the vertical lines result from the grating. (**B**) Depict oscillation maps. The *x*-axis represents the image pixels along the *x*-axis. For each pixel, local intensity oscillation over two grating period can be determined. The intensity is shown along the *y*-axis of the oscillation map. The label above the oscillation map denotes the image *y*-axis value. For example, the image edge at $(x, y) = (75, 41)$ in Figure 4A can be clearly identified in its corresponding oscillation map in Figure 4B.

DISCUSSION

For the first time, a grating interferometer was used to qualitatively examine cochlear tissue using two-dimensional X-ray phase radiography. The results suggest that hard X-ray phase imaging with grating interferometers can be applied in areas where phase imaging would be desirable, but is currently not widely used. Furthermore, the grating interferometer technique provides quantitative information about the phase shifts created by the imaged object. The demonstration of the phase shift by the soft tissue leads to the next challenge, imaging radiopaque and radiolucent structures at the same time; imaging cochlear soft tissue surrounded by bone.

Phase stepping presents a method to separate absorption from phase signal and to retrieve the projected phase, while preserving the resolution of the imaging system (Kottler et al., 2007; Pfeiffer et al., 2005; Weitkamp et al., 2005; Yashiro et al., 2008). With the present experiments, we have demonstrated that similar to previous groups we are able to retrieve phase information from a series of images obtained with coherent hard X-rays and a grating interferometer. A 20-µm slice of cochlear soft tissues shifts the phase by 120°, or $2/3\pi$.

Phase contrast imaging is desirable in medical diagnostics. However, it requires coherent hard X-rays, which are currently available at synchrotrons. Because there are fewer than 40 synchrotrons worldwide, the application of phase contrast imaging to medical diagnostics has not been widely used. Recent progress in

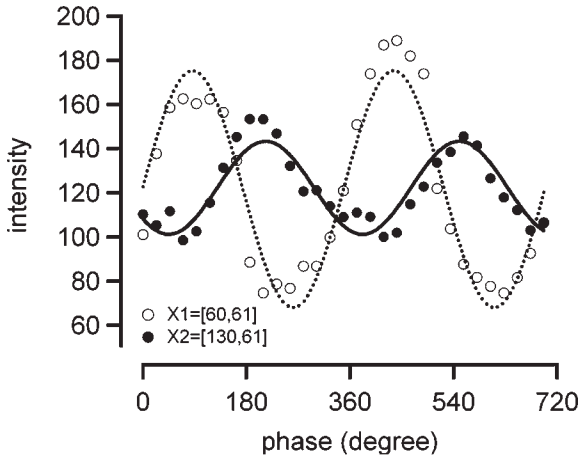

Fig. 5. Intensity profiles are shown for the different positions of the grating at image (x, y) coordinates (60, 61) and (130, 61) shown in Figure 4. One location has been selected on a soft tissue structure and the other location has no tissue in the beam. The phase difference between the two sites is about 120°.

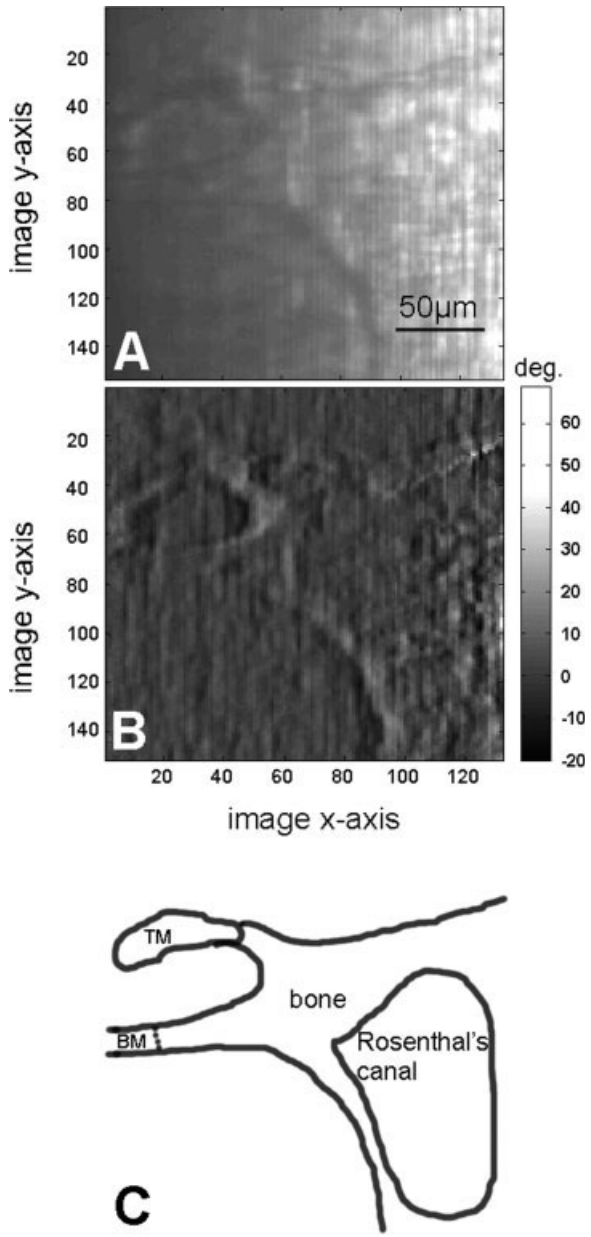

Fig. 6. Phase stepping. **A**: The image shows a cochlear cross section for an arbitrary constellation of the phase grating and the analyzer grating. **B**: For different relative positions of the two interferometer-gratings, the local oscillation in pixel intensity can be used to determine the phase ρ_i between neighboring pixels. The wavefront phase Φ has been retrieved from ρ_i by integration in the x-direction. The phase shift correlates with gray scale pixel intensity, according to the scale bars labeled "deg." **C**: A sketch of (A and B) indicating the structures that can be identified.

grating interferometer technology, however, promises to alleviate the dependency on synchrotrons to produce coherent X-rays, by converting broadband radiation into partially coherent radiation. The grating interferometer, therefore, will enable the use of broadband radiation as provided by laboratory X-ray generators with a reasonably compact setup to generate phase contrast images.

CONCLUSIONS

It is possible to image soft tissue structures with hard X-rays, and the use of grating interferometer can provide quantitative information about the phase shifts created by the imaged object in addition to yielding high-contrast images. The present experiments have demonstrated that a 20-μm slice of tissue obtained from the cochlea causes a phase shift of 60–120°, which corresponds to $1/3\pi$ to $2/3\pi$.

ACKNOWLEDGMENTS

The authors thank all the members of UNICAT for their support. They also thank Dr. R. Longo for providing information and for the discussion on the dosis calculation.

REFERENCES

Bunk O, Pfeiffer F, Stampanoni M, Patterson BD, Schulze-Briese C, David C. 2005. X-ray beam-position monitoring in the sub-micrometre and sub-second regime. J Synchrotron Radiat 12 (Pt 6):795–799.

David C, Nöhammer B, Solak HH, Ziegler E. 2002. Differential phase contrast imaging using a shering interferometer. Appl Phys Lett 81:3287–3289.

Guigay JP, Zabler S, Cloetens P, David C, Mokso R, Schlenker M. 2004. The partial Talbot effect and its use in measuring the coherence of synchrotron X-rays. J Synchrotron Radiat 11 (Pt 6):476–482.

Kottler C, Pfeiffer F, Bunk O, Grunzweig C, David C. 2007. Grating interferometer based scanning setup for hard X-ray phase contrast imaging. Rev Sci Instrum 78:043710.

Momose A, Takeda T, Itai Y, Yoneyama A, Hirano K. 1998. Phase-contrast tomographic imaging using an X-ray interferometer. J Synchrotron Radiat 5 (Pt 3):309–314.

Pfeiffer F, Bunk O, Schulze-Briese C, Diaz A, Weitkamp T, David C, van der Veen JF, Vartanyants I, Robinson IK. 2005. Shearing interferometer for quantifying the coherence of hard X-ray beams. Phys Rev Lett 94:164801.

Pfeiffer F, Grunzweig C, Bunk O, Frei G, Lehmann E, David C. 2006a. Neutron phase imaging and tomography. Phys Rev Lett 96:215505.

Pfeiffer F, Weitkamp T, Bunk O, David C. 2006b. Phase retrieval and differential phase contrast imaging with low-brilliance X-ray sources. Nature 2:258–261.

Rau C, Robinson IK, Richter CP. 2006. Visualizing soft tissue in the mammalian cochlea with coherent hard X-rays. Microsc Res Tech 69:660–665.

Snigirev A, Snigireva I, Kohn V, Kuznetzov S, Schelokov I. 1995. On the possibilities of X-ray phase contrast microimaging by coherent high-energy synchrotron radiation. Rev Sci Instrum 66:5486–5492.

Spanne P, Raven C, Snigireva I, Snigirev A. 1999. In-line holography and phase-contrast microtomography with high energy X-rays. Phys Med Biol 44:741–749.

Takeda T, Momose A, Itai Y, Wu J, Hirano K. 1995. Phase-contrast imaging with synchrotron X-rays for detecting cancer lesions. Acad Radiol 2:799–803.

Takeda T, Momose A, Yu Q, Wu J, Hirano K, Itai Y. 2000. Phase-contrast X-ray imaging with a large monolithic X-ray interferometer. J Synchrotron Radiat 7 (Pt 4):280–282.

Takeda T, Momose A, Wu J, Yu Q, Zeniya T, Thet-Thet L, Yoneyama A, Itai Y. 2002a. Vessel imaging by interferometric phase-contrast X-ray technique. Circulation 105:1708–1712.

Takeda T, Yoneyama A, Momose A, Wu J, Zeniya T, Lwin TT, Tsuchiya Y, Rao DV, Hyodo K, Hirano K, Aiyoshi Y, Itai Y. 2002b. Phase-contrast X-ray imaging with X-ray interferometer for medical applications. Igaku Butsuri 22:30–37.

Weitkamp T, Diaz A, David C, Pfeiffer F, Stampanoni M, Cloetens P, Ziegler E. 2005. X-ray phase imaging with a grating interferometer. Opt Expr 12:6296–6304.

Yashiro W, Takeda Y, Momose A. 2008. Efficiency of capturing a phase image using cone-beam X-ray Talbot interferometry. J Opt Soc Am A Opt Image Sci Vis 25:2025–2039.